Composites Part B 259 (2023) 110755

Contents lists available at ScienceDirect

Composites Part B

journal homepage: www.elsevier.com/locate/compositesb

Structural and damage analysis of a programmable shape memory locking laminate with large deformation

Zhengxian Liu [a], Tong Mu [b], Xin Lan [a], Hanxing Zhao [a], Liwu Liu [b], Wenfeng Bian [c], Yanju Liu [b,**], Jinsong Leng [a,*]

[a] Center for Composite Materials and Structures, Harbin Institute of Technology (HIT), Harbin, 150080, PR China
[b] Department of Astronautical Science and Mechanics, Harbin Institute of Technology (HIT), Harbin, 150001, PR China
[c] Department of Civil Engineering, Harbin Institute of Technology (HIT), Weihai, 264209, PR China

ARTICLE INFO

Handling Editor: Dr Hao Wang

Keywords:
Shape memory polymer composites
Locking laminate
Large deformation
Damage analysis

ABSTRACT

Smart structures based on shape memory polymer composites (SMPCs) are gradually applied to the aerospace field hosting an ideal combination of properties. The damage behavior of SMPC-based smart structures with large deformations requires mechanism research to satisfy their reliability. In this study, a programmable SMPC-based locking laminate was investigated, which is expected to replace initiating explosives. Firstly, based on fiber buckling theory, fiber-reinforced SMPC locking laminate was designed and analyzed, and the safe allowable area and damage modes were determined. Additionally, the deformation test of the locking laminate based on fiber fabric reinforced SMPC showed that there is two typical damage behavior: matrix cracking and interlayer delamination. For this reason, theoretical analysis was performed to reveal the damage mechanism and initial damage location. The results indicated that the fiber bundle width, arc radius, and thickness were the influencing factors of matrix cracking, while the center angle was the influencing factor of delamination. Finally, finite element analysis shows the validity of the theoretical analysis. This research has potent inspiration and reference significance for the design of SMPC-based smart structures.

1. Introduction

Shape memory polymers (SMPs) [1–3] are a class of smart materials that can transform from their original shape to a temporary shape through external stimulation (thermal stimulation, electrical stimulation, magnetic stimulation, etc) [4–7]. The thermal-responsive SMPs exhibit different mechanical properties at different temperatures [8–10]. They are in a rubbery state with low modulus and high elongation at break when the external temperature rises to the glass transition temperature (T_g) [11,12]. Hence, they can easily be endowed with complex shapes at this time. After the temperature drops, the material can maintain its temporary shape while regaining its original modulus and strength. However, adding a reinforcing phase can improve mechanical properties and broaden the application scope [12–15].

SMPC generally has large deformation problems during shape programming. The large deformation bending behavior of SMPC has been preliminarily studied [16]. Francis et al. [17] used an energy method to develop a mechanical model of fiber buckling in a unidirectional fiber-reinforced SMPC and quantified the wavelength and amplitude of the fiber. Lan et al. [18,19] investigated the deformation behavior of fiber buckling during bending by taking into account the compressing and buckling area and discovered the fiber buckling fracture damage mode. Gall et al. [20] found out-of-buckling behavior during the deformation test of fabric-reinforced SMPC, and there are damage modes such as fiber buckling fracture and delamination.

Shape memory polymer composites (SMPCs) have a wide range of applications in space locking and deployment mechanisms due to their excellent mechanical properties, low impact, and controllable deformation capabilities [21,22]. Epaarachchi et al. [23] developed a deployable spatial habitat based on SMPC that could be programmed to have a nearly threefold smaller volume and almost recover to its original shape under vacuum conditions. Zhao et al. [24] used filament winding technology to create an SMPC-based large load-bearing separation device that had no impact during the release process. Leng et al. [25]

* Corresponding author.
** Corresponding author.
E-mail addresses: yj_liu@hit.edu.cn (Y. Liu), lengjs@hit.edu.cn (J. Leng).

https://doi.org/10.1016/j.compositesb.2023.110755
Received 3 November 2022; Received in revised form 13 April 2023; Accepted 16 April 2023
Available online 17 April 2023
1359-8368/© 2023 Elsevier Ltd. All rights reserved.

designed an SMPC-based locking laminate structure, which has been applied to an SMPC-based flexible solar array. The solar array was assembled to the SJ-20 Geosynchronous Satellite and launched into geosynchronous orbit with Long-March-5 Y3 Heavy Rocket, and the on-orbit locking and release functions were successfully demonstrated. Despite some progress in understanding the large deformation behavior of SMPC-based structures, a thorough study of the damage mechanisms and damage modes during large deformation of SMPC is still lacking. These perceptions are especially important for SMPC-based structure design and damage analysis.

In this study, the structural and damage analysis of a programmable SMPC-based locking laminate with large deformation was carried out. Firstly, using fiber buckling theory, the structural analysis of the locking laminate based on unidirectional fiber-reinforced SMPC was performed. Two damage modes of matrix cracking and interlayer delamination were found during the deformation test of locking laminate based on fiber fabric-reinforced SMPC. The effects of these two damage states on shape memory performance were further investigated. Then, the damage mechanism, initial damage location and influencing factors were determined through the stress state analysis of the matrix in the interlayer and compression zones. Finally, the ABAQUS software was used to develop the structural model and representative volume element (RVE) model to simulate and verify the stress state of the matrix in the interlayer and compression zones.

2. Structure analysis and fabrication

2.1. Structure analysis

A locking laminate based on fiber-reinforced SMPC was designed and analyzed in the study. The locking laminate is made up of three arc segments and two linear segments, with a Ω-shape cross-section (as shown in Fig. 1(a)). Thickness (t), linear segment (d), width (w), arc radius (r), and center angle (θ) were used to determine the geometric model. The arc segment design reduced the stress concentration during deformation and effectively increased the release stroke. The shape memory cycle of the locking laminate is shown in Fig. 1(b).

The locking laminate based on unidirectional fiber-reinforced SMPC was analyzed by considering fiber buckling. When the unidirectional fiber-reinforced SMPC is bent at Tg, the shear modulus of the matrix in the compressing area is insufficient to resist transverse deformation of the fiber, and the fiber buckles (as shown in Fig. 2), according to the related literature [18,19]. The cross-section can be divided into three areas based on the stress state of the fiber (as shown in Fig. 2(c)), and the matrix and fiber deformation diagram in the X–Y plane is shown in Fig. 2 (d) z_{cb} and z_{ns} represent the critical buckling position and neutral surface position, respectively.

When the fiber buckles, the geometric shape presents sinusoidal/cosine waves, and the shape function of the buckling fiber is as follows:

$$y = \frac{2\lambda}{\pi}\sqrt{\kappa(z_{ns}-z)}\cos\left(\frac{\pi x}{\lambda}\right) \tag{1}$$

where λ denotes the half-wavelength of the buckling fiber, and κ denotes bending curvature. According to the deformation state analysis of the matrix and fiber, the matrix deformation includes the tensile and compression deformations in the X-direction, the shear deformations in the X–Y plane, and the Y-Z plane in the buckling region. The fiber deformation includes buckling, tensile and compression deformations. The stress of the matrix and fiber in the non-buckling region is expressed as follows:

$$\sigma_{mxx} = E_m\varepsilon_{mxx} = E_m\kappa(z-z_{ns}) \tag{2}$$

$$\sigma_{fxx} = E_f\varepsilon_{fxx} = E_f\kappa(z-z_{ns}) \tag{3}$$

where E_m and E_f represent the modulus of matrix and fiber, respectively. When $z = t$, the stress of the fiber reaches the maximum:

$$\sigma_{fxx,\max} = E_f\kappa(t-z_{ns}) \tag{4}$$

According to the equal strain assumption of the matrix and fiber, the shear stress τ_{xy} of the matrix is expressed as follows:

$$\tau_{xy} = -G_m\sqrt{\kappa(z_{ns}-z)}\sin\left(\frac{\pi x}{\lambda}\right) \tag{5}$$

where G_m denotes the shear modulus of the matrix. When $z = 0$, $x = n\lambda/2$ ($n = 0,1,2\cdots\cdots$), the shear stress τ_{xy} reaches the maximum:

$$\tau_{xy,\max} = 2G_m\sqrt{\kappa z_{ns}} \tag{6}$$

The amplitude of the fiber in the Z-direction varies according to the shape function of the fiber, resulting in the shear stress of the matrix in the Y-Z plane. The matrix's shear stress τ_{yz} is expressed as follows:

$$\tau_{yz} = G_m\gamma_{yz} = G_m\frac{\delta y}{\delta z} = \frac{G_m\kappa\lambda}{\pi\sqrt{\kappa(z_{ns}-z)}}\cos\left(\frac{\pi x}{\lambda}\right) \tag{7}$$

When $z = z_{cb}$, $x = n\lambda$ ($n = 0,1,2\cdots\cdots$), the shear stress τ_{yz} reaches the maximum:

$$\tau_{yz,\max} = \frac{G_m\kappa\lambda}{\pi\sqrt{\kappa(z_{ns}-z_{cb})}} \tag{8}$$

Although the stress state analysis of the matrix in the buckling area, the maximum stress occurs at $z = 0$ or $z = z_{cb}$. When $x = n\lambda/2$ (n = 0,1,2……), the maximum shear stress of the matrix at $z = 0$ is expressed

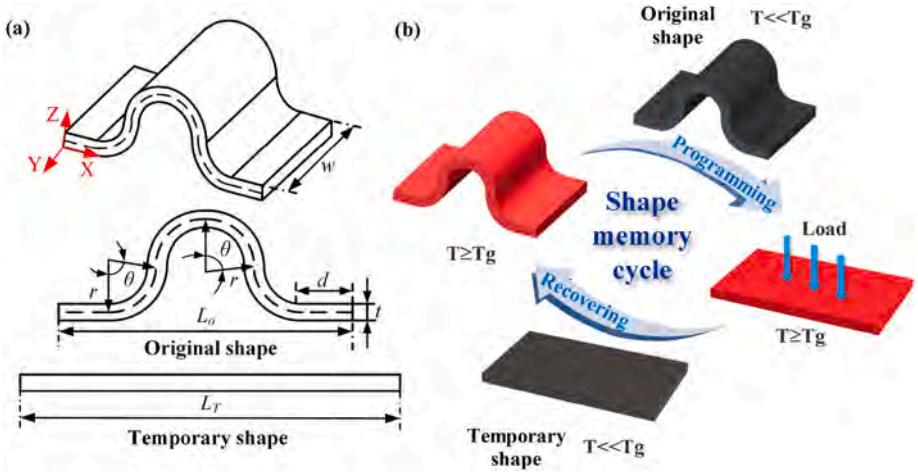

Fig. 1. (a) Locking laminate model; (b) shape memory cycle of the locking laminate.

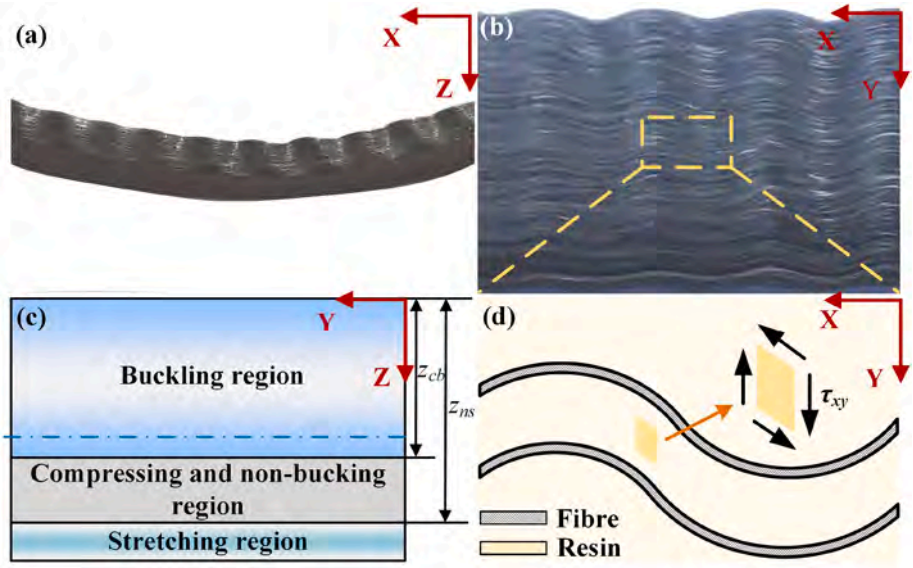

Fig. 2. Deformation diagram of the unidirectional fiber-reinforced SMPC: (a) X-Z view; (b) X–Y view; (c) cross-section subarea; (d) deformation diagram of matrix and fiber in the X–Y plane.

as follows:

$$\tau_{z=0,\max} = 2G_m\sqrt{\kappa z_{ns}} \tag{9}$$

When $x = n\lambda$ ($n = 0,1,2\cdots\cdots$), the maximum shear stress of the matrix at $z = z_{cb}$ is described as follows:

$$\tau_{z=z_{cb},\max} = \frac{G_m\kappa\lambda}{\pi\sqrt{2C}} \tag{10}$$

where $C = \nu_m G_m/(\nu_m E_m + \nu_f E_f)$. Buckling deformation is the fiber's deformation mode in the buckling area. The curvature of the fiber can be expressed as follows:

$$\kappa_f = \frac{|y''|}{(1+y'^2)^{\frac{3}{2}}} = \frac{\left|\frac{A\pi^2}{\lambda^2}\cos\left(\frac{\pi x}{\lambda}\right)\right|}{\left[1+\frac{A^2\pi^2}{\lambda^2}\sin^2\left(\frac{\pi x}{\lambda}\right)\right]^{\frac{3}{2}}} \tag{11}$$

where A is the amplitude of the buckling fiber. The amplitude of the fiber is the maximum at $z = 0$. Simultaneously, when $x = n\lambda$ ($n = 0,1,2\cdots\cdots$), the curvature reaches its maximum. As a result, the maximum stress of the fiber buckling is expressed as follows:

$$\sigma_{f,\max} = E_f\varepsilon_{f,\max} = \frac{E_f dA\pi^2}{2\lambda^2} \tag{12}$$

where d denotes the diameter of the fiber. According to the related research [18,19], when the SMPC is undamaged, the expression of the neutral surface position, critical buckling position and half-wavelength can be described as follows:

$$z_{ns} = t - \frac{C}{\kappa}\left(\sqrt{1+\frac{2\kappa t}{C}} - 1\right) \tag{13}$$

$$z_{cb} = z_{ns} - \frac{2C}{\kappa} \tag{14}$$

$$\lambda = \left[\frac{8\pi^3\nu_f E_f I_f\left(z_{ns}{}^2 - \frac{4C^2}{\kappa^2}\right)}{\nu_m G_m d^2 \ln\left(\frac{z_{ns}\kappa}{2C}\right)}\right]^{\frac{1}{4}} \tag{15}$$

where ν_m and ν_f denote the volume content of the matrix and fiber, respectively. I_f denotes the cross-section moment of inertia of the fiber.

The locking laminate transforms from an arc shape to a flat shape (as shown in Fig. 1(b)), which can be regarded as the reverse process of bending from a flat shape to an arc shape. Thus, the maximum neutral surface and critical buckling positions of the arc segment are expressed as follows:

$$\begin{cases} z_{ns} = t - rC\left(\sqrt{1+\frac{2t}{rC}} - 1\right) \\ z_{cb} = z_{ns} - 2rC \end{cases} \tag{16}$$

Because the matrix and fiber are primarily subjected to shear and tensile stress at the dangerous points, the maximum shear stress and maximum tensile stress criterion were used to assess matrix and fiber damage. According to the stress analysis of the matrix and fiber, the matrix's dangerous point is at the compressing and buckling surface ($z = 0$) and critical buckling surface ($z = z_{cb}$), while the fiber's dangerous point is at the maximum fiber buckling ($z = 0$) and the tensile surface ($z = t$). The stress of the matrix and fiber must be less than their respective strengths. As a result, the stress at the dangerous points must meet the following conditions:

$$\tau_{z=0,\max} \le \tau_s, \tau_{z=z_{cb},\max} \le \tau_s, \sigma_{f,\max} \le \sigma_{sf}, \sigma_{fcx,\max} \le \sigma_{sf} \tag{17}$$

where τ_s represents the shear strength of the matrix, and σ_{sf} represents the tensile strength of the fiber. The maximum arc radius corresponding to the above stresses was used as the critical damage radius:

$$r_{cf} = \max\left\{r_{z=0,\max}, r_{z=z_{cb},\max}, r_{f,\max}, r_{fcx,\max}\right\} \tag{18}$$

Fig. 3 shows the critical relationship curve in the design between the arc radius and the thickness. The safe allowable arc and thickness areas are above the critical damage curves. The material parameters used in the study are shown in Table 1. The arc radius corresponding to critical damage moves upward as the thickness increases, indicating that the thickness is positively correlated with the arc radius of critical damage. At the same time, as the fiber volume content increases, so does the arc radius corresponding to critical damage.

Theoretical analysis of the deformation of unidirectional fiber-reinforced SMPC has studied in previous works. However, the previous studies were mainly based on bending analysis without damage which are not suit for Ω-shape structure, and the theoretical analyses were rarely applied to the design and analysis of SMPC-based structures

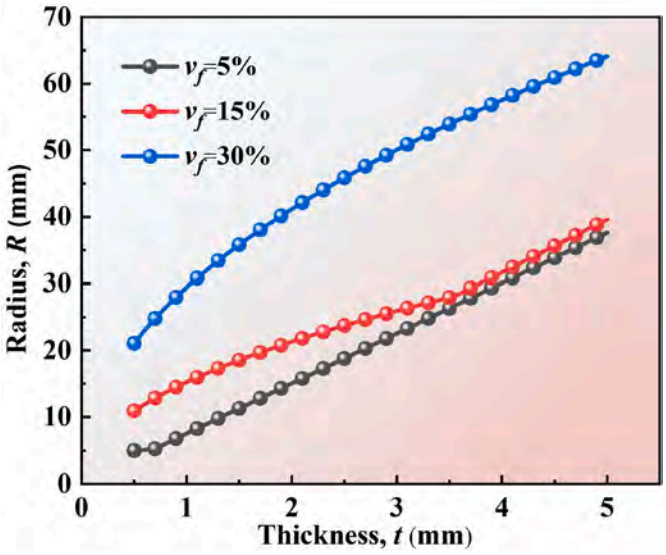

Fig. 3. Critical relation curve between arc radius and the thickness during the structural design.

Table 1
Material parameters of matrix and carbon fiber.

Material	Tensile modulus (MPa)	Shear modulus (MPa)	Poisson's ratio	Shear strength (MPa)	Tensile strength (MPa)
Resin (T_g)	32	11	0.45	7.8	8.2
fiber	230,000	–	0.3	–	3530

[18,26]. The present study further analyzed the damage mechanism and damage limit based on the previous study and applied it to the design and analysis of the Ω-shape locking laminate. This study can provide a reference for the design and analysis of SMPC-based structures.

Table 2 lists the minimum allowable arc radius and corresponding damage modes for various fiber volume content and thickness. When the thickness is 1 mm and fiber volume content is 30%, the arc radius must be greater than 22.56 mm to ensure structural safe. The damage morphology under these three damage modes during unidirectional fiber-reinforced SMPC bending is shown in Fig. 4.

2.2. Material fabrication

Unidirectional fiber-reinforced and fabric-reinforced SMPC are commonly used in space deployable and lock release structures. The deployable structures based on unidirectional fiber-reinforced SMPC can be designed and analyzed using the fiber buckling model. However, fabric-reinforced SMPC lacks a deformation theoretical model to guide structural design and analysis. As a result, the structure based on fabric-reinforced SMPC can currently only be studied experimentally. This study began with an experiment to determine the damage locations and damage modes, followed by theoretical analysis to determine the initial damage location and damage mechanism, and finally the influencing factors.

Table 2
Minimum allowable arc radius and corresponding damage modes under different fiber volume content and thickness.

Thickness (mm)	Minimum arc radius (mm) (damage mode)		
	fiber volume content (5%)	fiber volume content (15%)	fiber volume content (30%)
1	7.52 (fiber buckling fracture)	15.04 (Delamination)	22.56 (Delamination)
2	15.25 (Matrix cracking)	21.30 (Delamination)	25.92 (Delamination)
3	29.43 (Matrix cracking)	41.13 (Delamination)	50.85 (Delamination)
4	30.08 (Matrix cracking)	31.66 (Matrix cracking)	67.53 (Delamination)

The shape memory resin adopted in this study was developed by Leng's group [27]. Toray T300-3 k carbon fiber twill was used for reinforcement. The number of fiber laying layers was 4, with a 45° layup direction and a 30% fiber volume content. The compression molding technique (CMT) was adopted to control the fiber volume content. The dimensions of the parameters are as follows: $t = 1.5$ mm, $R = 4.39$ mm, $d = 5$ mm, $L_s = 10$ mm, $w = 21$ mm, $\theta = 90°$.

3. Experimental

3.1. Dynamic mechanical analysis

The locking laminate is a kind of thermal-responsive SMPC that exhibits various mechanical properties at different temperatures. The dynamic thermodynamic properties of shape memory materials were evaluated using dynamic mechanical analysis (DMA). Since the deformation mode of the locking laminate was mainly bending, the three-point bending mode was adopted in this study. The specimen dimensions were 13.94 mm × 6.00 mm × 1.98 mm. The temperature range was 20–200 °C with a heating rate of 3 °C/min, and the loading frequency was 1 Hz.

3.2. Deformation and damage observation

The damage morphology of the locking laminate was observed by the deformation test. The deformation test was completed using a compression testing machine equipped with a temperature chamber. During a deformation cycle, the damage location and morphology of the locking laminate were observed. Following that, multiple deformation cycles were performed to observe the delamination's propagation.

3.3. Recovery performance test

Multiple recovery performance tests were performed on the locking laminate to investigate the effect of damage on recovery performance. The recovery ratio can be described as Eq. (19). Where L_R denotes the length after recovery. The locking laminate was recovered in a temperature chamber of 150 °C. During the test, one end was fixed while the other could freely recover. In addition, in order to demonstrate its locking and releasing process, the locking laminate was equipped with a locking mechanism to test its recovery performance. The locking laminate was provided thermal stimulation by pasting a heating film on the surface, and the heating film power was 4.2 W.

$$R_f = \frac{L_T - L_R}{L_T - L_o} \times 100\% \tag{19}$$

4. Results and discussion

4.1. Dynamic mechanical properties

The variation of the storage modulus and Tan δ of the materials with temperature is shown in Fig. 5. As the temperature rose, the storage modulus of the material decreased gradually. This is due to the gradual activity of the molecular chains within the epoxy resin and the gradual transition of the material from the glassy state to the rubbery state. The material softens and the modulus gradually decreases in macroscopic appearance. The Tg of SMP and SMPC were 150 °C and 123 °C, respectively. The modulus of SMP and SMPC at 150 °C was 35.4 times

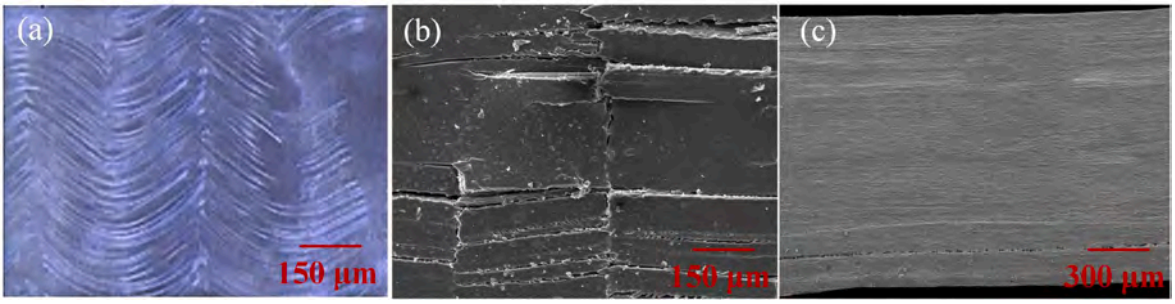

Fig. 4. Damage morphologies of the unidirectional fiber-reinforced SMPC during bending: (a) fiber buckling fracture; (b) matrix cracking; (c) delamination.

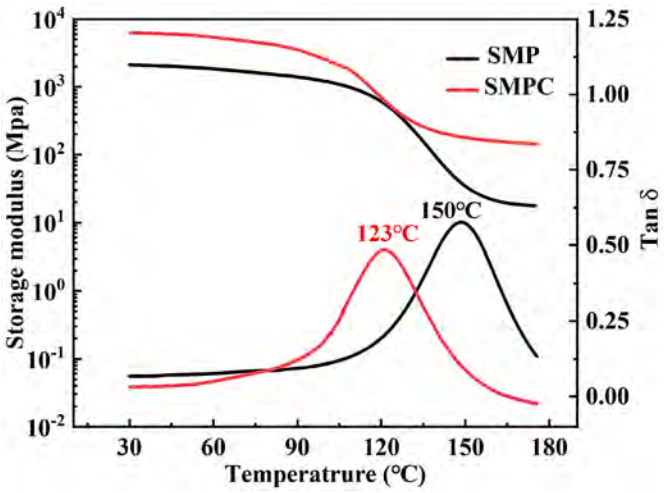

Fig. 5. DMA test curve of shape memory material.

and 65.6 times that of at 25 °C, respectively. As a result, it can easily be endowed with a complex shape at Tg.

4.2. Damage observation and analysis

Two morphological damage modes occurred in the locking laminate during the deformation process. Fig. 6 shows the surface morphology of the locking laminate in the compressing zone and interlaminar. The matrix cracking occurred in the compressing zone at the intersection of the fiber bundles. The preliminary analysis may be due to the torsional deformation of the fiber bundle laid at ±45° under the compressive load, which leads to matrix shear deformation. The delamination damage was discovered on the surface morphology of the locking laminate. This is due to the fact that when the SMPC is bent, interlaminar shear deformation causes delamination. The damage mechanism and initial damage location would be revealed through theoretical analysis in the fifth section. Fig. 7 presents the morphology in the thickness direction after undergoing 0, 1, 3, and 5 deformation cycles. Delamination cracks grew gradually as deformation times increased.

In the previous study on fabric-reinforced SMPCs, only matrix cracking damage was observed [20]. When comparing our results to the previous study, it must be pointed out the reason of lack of delamination damage is that the previous fabric-reinforced SMPC was very thin and the number of layers of fiber fabric was single layer. In this work, the four-layer fabric reinforced SMPC was selected and then the interlayer delamination damage was also observed under bending. The damage mechanism of fiber fabric-reinforced SMPC can be further understood through the following theoretical analysis. These findings have some guiding significance for our deformation analysis and structural design for some fabric-reinforced SMPC structures.

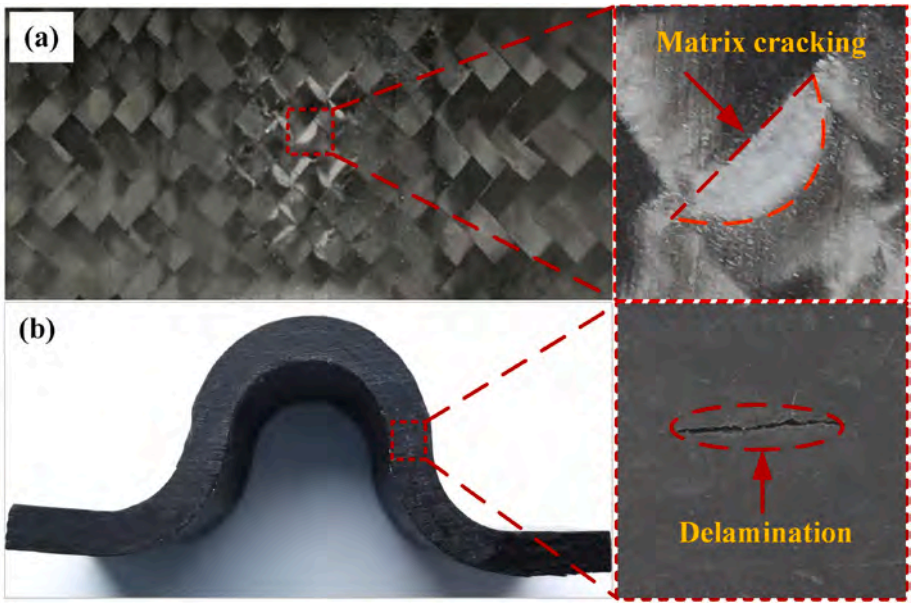

Fig. 6. Surface morphology of the locking laminate: (a) surface morphology of the compression zone; (b) surface morphology of the interlamination.

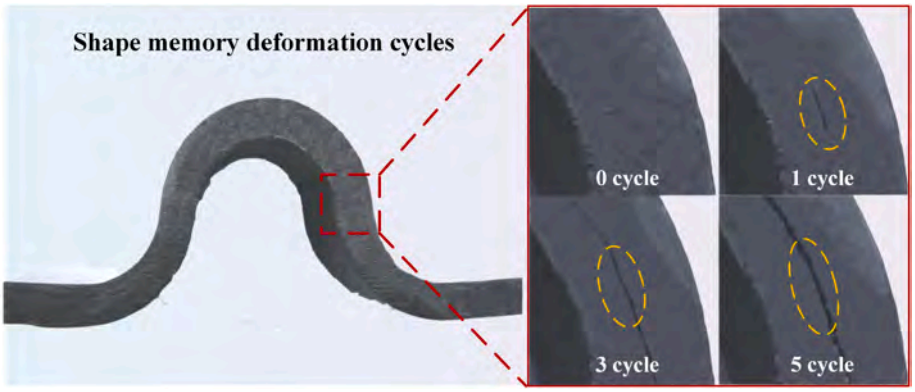

Fig. 7. Morphology in the thickness direction after 0, 1, 3, and 5 thermomechanical cycles.

4.3. Recovery performance

The initial recovery process of the locking laminate is shown in Fig. 8 (a). The locking laminate could be recovered within 120 s. Fig. 8(b) shows the recovery ratio of the first 10 times of the locking laminate. According to the data, the initial recovery ratio could reach 97%. As the deformation times increased, the internal damage became more severe, and the recovery ratio decreased. After 10 times deformations, the recovery ratio could still be maintained above 90%. The damage had no negative impact on the recovery performance. This is because the internal damage was at the physical level and had no effect on shape memory performance.

Fig. 9 shows the recovery process of the SMPC-based locking laminate installed on the locking mechanism. The locking laminate and the locking part were installed together in the locked state, and the structure was locked by axial positioning and axial force. When the release is required, the material slowly recovers to its original shape upon reheating, which drives the axial recovery of the locking mechanism to realize the release of the structure. The locking mechanism can complete the release action in 180 s. Notably, the SMPC-based locking laminate designed based on the theoretical analysis in this study has successfully achieved in-orbit locking and release of the flexible solar array system for the first time in the world [25]. The SMPC-based locking laminate has the advantages of light-weight, large deformation, and low impact, which will become a suitable candidate for the locking device of the small satellite. In the future, the SMPC-based locking mechanism will provide new ideas and methods for the design of space locking-releasing mechanisms.

5. Theoretical analysis

During the deformation process of a locking laminate based on fiber fabric-reinforced SMPC, two damage modes were observed: interlayer delamination and matrix cracking. The stress state of the two damage locations was theoretically analyzed based on experimental evidence. Fig. 10 shows the deformation analysis diagram of a 1/2 cross-section of locking laminate. The shaded area represents the carbon fiber layer, the white area is the matrix, and the black area is the matrix's micro-element body. As we all know, the resin is in a rubbery state during the deformation process, and its stiffness is much lower than that of the fiber. Because the deformation of the straight section is very small, it is assumed that the shear strain of the straight section is negligible. Comparing the matrix deformation, it was discovered that the micro-element body of the interlayer matrix changed from square to diamond, indicating shear deformation in the interlayer matrix.

The geometric relationship (as shown in Eq. (20)) before and after the deformation of the micro-element body can be used to calculate the shear strain expression of the interlayer matrix (as shown in Eq. (21)).

$$\tan\gamma = \frac{\psi(R+h) - \psi R}{h} = \psi \tag{20}$$

$$\gamma = \arctan\psi \tag{21}$$

When θ reaches the maximum value, the corresponding shear strain reaches the maximum value.

$$\gamma_{max} = \arctan\theta \tag{22}$$

The release stroke of the locking laminate must be considered to realize the release function of the locking laminate. The release stroke can be expressed as follows:

$$\triangle L = 4(\theta - \sin\theta)r \tag{23}$$

To obtain the variation of the release stroke with the central angle, let $r = 1$, and the expression can be changed to:

$$\triangle L = 4(\theta - \sin\theta) \tag{24}$$

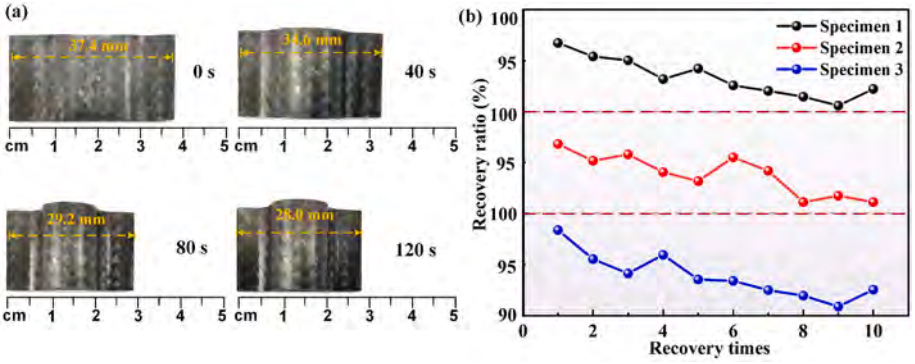

Fig. 8. Recovery performance of the locking laminate (a) initial recovery process; (b) recovery ratio.

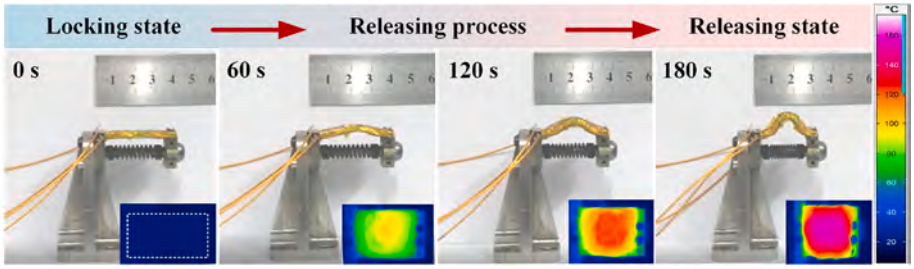

Fig. 9. Recovery process of the locking laminate in the locking mechanism.

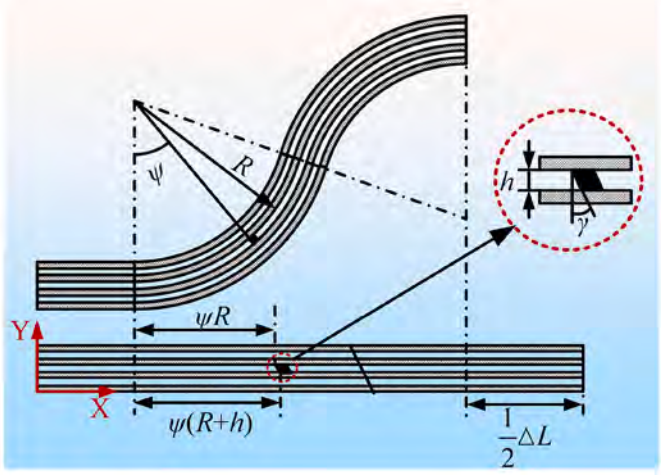

Fig. 10. Deformation analysis diagram of 1/2 cross-section of locking laminate.

Fig. 11 shows the variation of the maximum shear strain and release stroke with the central angle. The increasing rate of the maximum interlaminar shear strain decreases as the central angle increases, while the increasing rate of the release stroke increases. The interlayer shear stress and release stroke can be changed during structural design by adjusting the central angle. The angle change of the micro element is consistent with the center angle. The maximum interlayer shear strain in this study is 1.004 without considering the damage. The results demonstrated that the shear deformation of the interlayer matrix is the damage mechanism of interlayer delamination, that the initial damage location occurs at the arc transition position, and that the central angle is the damage influence factor.

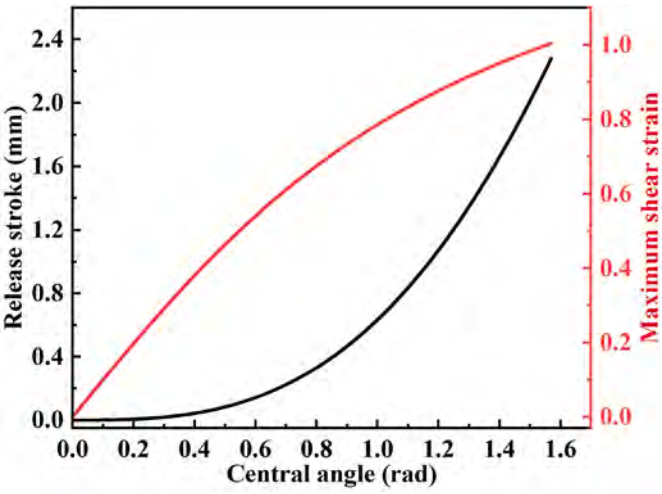

Fig. 11. Variation of the maximum shear strain and release stroke with the central angle.

Then, the matrix stress state in the compressing region was analyzed. The carbon fiber twill in the locking laminate was laid at an angle of ±45°. When the locking laminate was bent, the cross-section was divided into compressing region and stretching region. Because the fiber bundle was wavy (as shown in Fig. 12(a)), it was gradually straightened in the tensile zone, increasing the tensile region's bending stiffness. As a result, the neutral surface position would shift to the tensile surface, and the compressing region would experience greater strain than the stretching region. Fig. 12(b) and c are the stress analysis of the fiber overlap in the compressing region. Because the matrix stiffness was much lower than the fiber stiffness, relative torsion between the upper and lower fiber bundles occurred frequently during compression deformation (as shown in Fig. 12(d), causing matrix shear in the overlapping part.

When relative torsion occurs between the fiber bundles, the stress function [28] of the matrix where the fiber bundles overlap can be expressed as follows.

$$\varphi = G_m K\left[\frac{b^2}{4} - y^2 - \frac{8b^2}{\pi^3}\sum_{m=1,3,5\cdots}^{\infty}\frac{(-1)^{\frac{m-1}{2}}\cosh\frac{m\pi x}{b}\cos\frac{m\pi y}{b}}{m^3\cosh\frac{m\pi}{2}}\right] \tag{25}$$

where φ denotes the stress function, G_m denotes the shear modulus of the matrix, K denotes the relative rotation angle per unit length and b denotes the side length. According to the membrane analogy [29], the maximum shear stress occurs at the midpoint of the square side. The shear stress reaches the maximum when $x = 0$ and $y = -b/2$.

$$\tau_{\max} = \frac{\partial\varphi}{\partial y}\Big|_{x=0,y=\frac{b}{2}} = G_m K b\left[1 - \frac{8}{\pi^2}\sum_{m=1,3,5\cdots}^{\infty}\frac{1}{m^2\cosh\frac{m\pi}{2}}\right] \tag{26}$$

Eq. (26) shows that the matrix shear stress is positively correlated with the side length of the overlapping fiber bundle and the relative rotation angle between the fiber bundles. Because the side length of the overlapping area of the fiber bundle is consistent with the width of the fiber bundle, a narrow fiber bundle can reduce the shear stress of the matrix. At the same time, the relative rotation angle of the fiber bundles is positively correlated with the compressive strain, which is positively correlated with the thickness and negatively correlated with the arc radius. As a result, by adjusting the arc radius and thickness, shear stress can be reduced. Theoretical analysis reveals that the torsional deformation of the matrix in the middle of the fiber bundles is the damage mechanism of matrix cracking, and the maximum shear strain occurs in the middle of the fiber bundle edge in the overlapping area. The main influencing factors of matrix cracking are fiber bundle width, arc radius, and thickness.

6. Finite element analysis

The delamination damage and stress state of the locking laminate were analyzed using ABAQUS software to validate the theoretical analysis and experimental results. The finite element model of the

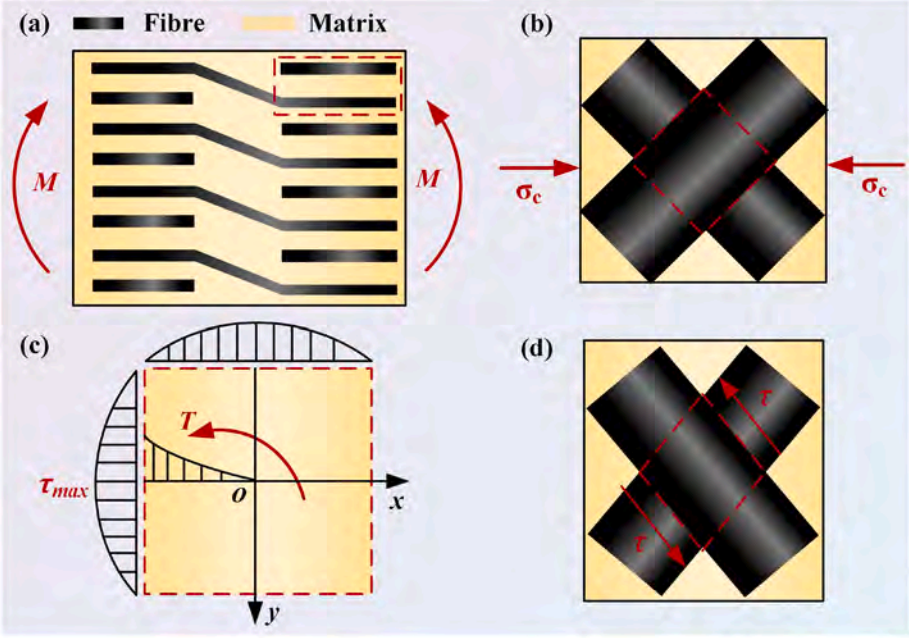

Fig. 12. Stress analysis on the compressing zone of the locking laminate.

locking laminate is shown in Fig. 13(a). The material parameters used in the model are listed in Table 3. The model consists of 4 composite material layers and 3 cohesive element layers, each with a thickness of 0.4 mm and 0.01 mm. In the simulation, the upper and lower pressure plates were set as rigid bodies, and the load was controlled by displacement. In this study, the quadratic stress initiation criterion was used to predict the damage initiation, and the cohesive zone model was used to simulate delamination damage.

The RVE of the single-layer composite was determined to simulate the matrix stress state in the compression zone (as shown in Fig. 13(b)). The fiber bundles were defined as having an elliptical shape. The fiber bundles' long axis distance was 1.6 mm, their short axis distance was 0.15 mm, and their spacing was 0.3 mm.

Fig. 14 shows the progressive damage of the middle cohesive element layer at different compression displacements. The results show that the initial damage location occurred in the arc transition section, which is consistent with the theoretical calculation results. When the compression displacement reached 8.94 mm, the cohesive element of the interlayer began to damage at the arc transition position. The damage increased as the compression displacement increased. Fig. 15(a) shows the simulation and theoretical results of interlaminar shear strain without considering delamination damage. The simulation result agreed well with the theoretical result. The interlayer shear stress was greatest at the arc transition position, which corresponded to the initial damage location. Fig. 15(b) shows the shear strain curve of the matrix at the fiber bundle overlap (selected area in the figure) in RVE. In the absence of damage, the matrix shear stress was greatest at the midpoint of the fiber bundle edge, gradually decreasing on both sides and eventually approaching zero, as predicted by the theoretical analysis. In addition, due to the potential limitations of ABAQUS software, we are unable to provide more comprehensive results. However, some available papers can be referenced to supplement our findings, such as the works of Pineda et al. (2021) [30] and Carrera et al. (2020) [31], who utilized NASMAT and CUF software to conduct multi-scale and micromechanical analyses of structures. In future study, we will combine multiple finite element software to thoroughly analyze the deformation process of SMPC-based structures.

Table 3
The material parameters at T_g used in the locking laminate model.

Composite layer	$E_{11} = E_{22}$	E_{33}	ν_{12}	$\nu_{23} = \nu_{13}$	G_{12}	$G_{23} = G_{13}$
	213.2 MPa	50.6 MPa	0.43	0.32	17.1 MPa	36.2 MPa
Cohesive layer	K_n	$K_s = K_t$	$t0\ n$	$t0\ s = t0\ t$	G_n	$G_s = G_t$
	3200 N/mm^3	3200 N/mm^3	1.2 MPa	1.2 MPa	0.63 N/mm	0.12 N/mm

The influence of structural parameters is further investigated under two stress states without damage. In this study, the influence of parameter variations on the two stress states of the interlaminar and compression region was investigated by varying the central angle of the

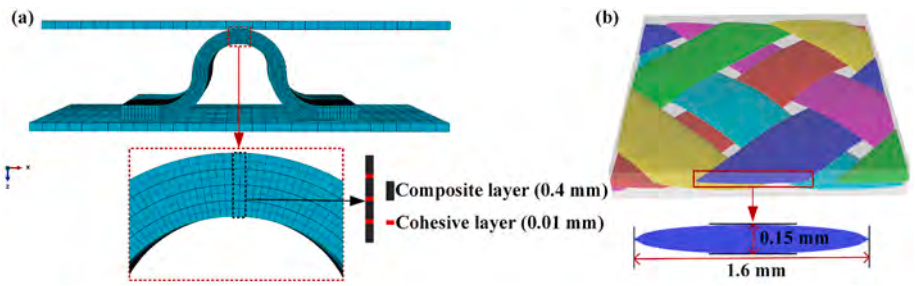

Fig. 13. Finite element model: (a) locking laminate model; (b) RVE model of the single-layer composite.

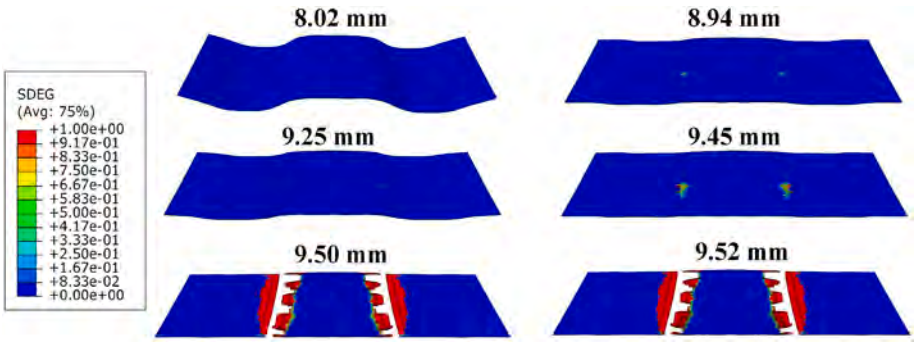

Fig. 14. Progressive damage of the middle cohesive element layer at different compression displacements.

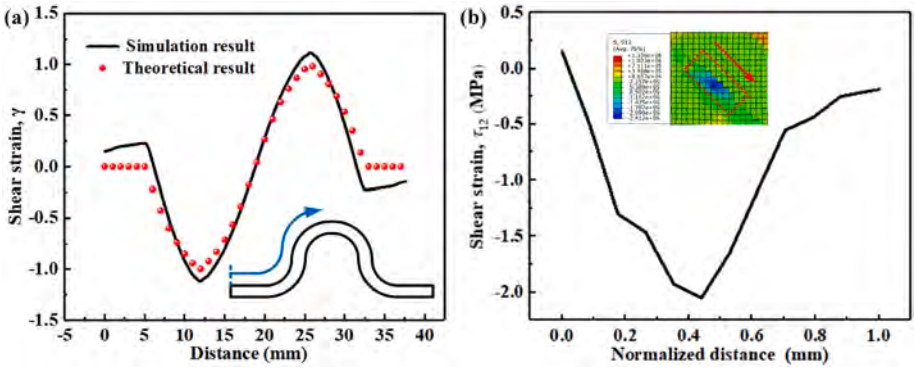

Fig. 15. Simulation results: (a) simulation and theoretical results of interlaminar shear strain without delamination damage; (b) matrix shear stress along the edge of the fiber bundle in the RVE.

circular segment of the locking laminate and the fiber bundle width inside the RVE. Table 4 shows the maximum interlaminar shear stress for each center angle. With the increase of the center angle, the maximum interlaminar shear stress gradually increased. Considering the assumption of the linear segment of the structure in the theoretical analysis, the relative error was within a reasonable range, and the simulation results were in good agreement with the theoretical results. Table 5 gives the maximum matrix shear stress along the edge of the fiber bundle with different width. It can be noted that the maximum matrix shear stress was positively correlated with the fiber bundle width, which also validated the conclusion given in Eq. (26). Due to the complexity of the matrix stress state in the compression region, detailed comparative analysis via the analytical solution proved difficult.

7. Conclusions

In this study, the structural and damage analysis of the SMPC-based locking laminate was investigated. The SMPC-based locking laminate designed based on the theoretical analysis has successfully achieved in-orbit locking and release of the flexible solar array system. Several conclusions are summarized below.

Table 4
Maximum interlaminar shear stress under different center angles without delamination damage.

Central angle		50°	60°	70°	80°	90°
Maximum interlaminar shear strain	Simulation results	0.758	0.870	0.956	1.035	1.116
	Theoretical results	0.717	0.808	0.884	0.949	1.000
Relative error		5.6%	7.7%	8.1%	9.1%	11.6%

Table 5
Maximum matrix shear stress along the edge of the fiber bundle under different fiber bundle width.

Fiber bundle width	0.5 mm	1 mm	1.5 mm	2 mm	2.5 mm
Maximum matrix shear stress	0.67 MPa	1.13 MPa	1.92 MPa	2.42 MPa	2.93 MPa

a) The fiber buckling theory was applied to the structural analysis of the locking laminate based on unidirectional fiber-reinforced SMPC, and the safe allowable area of arc radius and thickness was quantified for different fiber volume contents. During the deformation process, there are three major damage modes: delamination, matrix cracking, and fiber buckling fracture.
b) Delamination and matrix cracking are two common damage modes in locking laminates based on fiber fabric-reinforced SMPC. Furthermore, neither of the two damage modes resulted in irreversible damage to the shape memory performance. The recovery ratio could still be higher than 90% even after ten times of deformation.
c) The shear deformation of the interlaminar matrix was the damage mechanism of interlaminar delamination of a locking laminate based on fabric-reinforced SMPC. The central angle was the influencing factor of delamination. The matrix shear deformation at the overlap of fiber bundles was the matrix cracking damage mechanism. The fiber bundle width, arc radius and thickness were the influencing factors of the matrix cracking.

Author statement

I have made substantial contributions to the conception or design of the work; or the acquisition, analysis, or interpretation of data for the work. I have drafted the work or revised it critically for important

intellectual content. I agree to be accountable for all aspects of the work in ensuring that questions related to the accuracy or integrity of any part of the work are appropriately investigated and resolved.

I would like to declare on behalf of my co-authors that the work described was original research that has not been published previously, and not under consideration for publication elsewhere, in whole or in part. All the authors listed have approved the manuscript. We deeply appreciate your consideration of our manuscript, and we look forward to receiving comments from the reviewers. If you have any queries, please don't hesitate to contact me at the address below.

Declaration of competing interest

The authors declare that they have no known competing financial interests or personal relationships that could have appeared to influence the work reported in this paper.

Data availability

Data will be made available on request.

Acknowledgements

This work is supported by the National Natural Science Foundation of China (Grant No. 11632005, 11872020).

References

[1] Gopinath S, Adarsh N, Nair PR, Mathew S. One-way thermo-responsive shape memory polymer nanocomposite derived from polycaprolactone and polystyrene-block-polybutadiene-block-polystyrene packed with carbon nanofiber. Mater Today Commun 2020;22:100802.
[2] Lewis CL, Dell EM. A review of shape memory polymers bearing reversible binding groups. J Polym Sci, Part B: Polym Phys 2016;54(14):1340–64.
[3] Pilate F, Toncheva A, Dubois P, Raquez J-M. Shape-memory polymers for multiple applications in the materials world. Eur Polym J 2016;80:268–94.
[4] Lu H, Yin J, Xu B, Gou J, Hui D, Fu Y. Synergistic effects of carboxylic acid-functionalized carbon nanotube and nafion/silica nanofiber on electrical actuation efficiency of shape memory polymer nanocomposite. Int J Smart Nano Mater 2016; 100:146–51.
[5] Roth PJ, Lowe AB. Stimulus-responsive polymers. Polym Chem 2017;8(1):10–1.
[6] Yuan Z, Muliana A, Rajagopal K. Modeling deformation induced anisotropy of light-activated shape memory polymers. Int J Non Lin Mech 2020;120:103376.
[7] Zhang F, Wen N, Wang L, Bai Y, Leng J, Materials N. Design of 4D printed shape-changing tracheal stent and remote controlling actuation. Int J Smart Nano Mater 2021;12(4):375–89.
[8] Rossiter J, Takashima K, Scarpa F, Walters P, Mukai T. Structures. Shape memory polymer hexachiral auxetic structures with tunable stiffness. Smart Mater Struct 2014;23(4):045007.
[9] Hung P-y, Lau KT, Guo Q, Jia B, Fox B, Materials N. Tailoring specific properties of polymer-based composites by using graphene and its associated compounds. Int J Smart Nano Mater 2020;11(2):173–89.
[10] Zhang L, Huang Y, Dong H, Xu R, Jiang S. Flame-retardant shape memory polyurethane/MXene paper and the application for early fire alarm sensor. Compos B Eng 2021;223:109149.
[11] Li G, Wang AJ. Cold, warm, and hot programming of shape memory polymers. J Polym Sci B Polym Phys 2016;54(14):1319–39.
[12] Gu J, Zhang X, Duan H, Wan M, Sun H, Materials N. A hygro-thermo-mechanical constitutive model for shape memory polymers filled with nano-carbon powder. Int J Smart Nano Mater 2021;12(3):286–306.
[13] Karger-Kocsis J, Kéki S. Review of progress in shape memory epoxies and their composites. Polymers 2018;10(1):34.
[14] Mu T, Liu L, Lan X, Liu Y, Leng J. Shape memory polymers for composites. Compos Sci Technol 2018;160:169–98.
[15] Wang F, Wang W, Zhang C, Tang J, Zeng X, Wan X. Scalable manufactured bio-based polymer nanocomposite with instantaneous near-infrared light-actuated targeted shape memory and remote-controlled accurate self-healing. Compos B Eng 2021;219:108927.
[16] Bergman D, Yang B. A finite element model of shape memory polymer composite beams for space applications. Int J Numer Methods Eng 2015;103(9):671–702.
[17] Francis W, Lake M, Schultz M, Campbell D, Dunn M, Qi HJ. Elastic memory composite microbuckling mechanics: closed-form model with empirical correlation. In: Proceedings of 48th AIAA/ASME/ASCE/AHS/ASC structures, structural dynamics, and materials conference; 2007.
[18] Lan X, Liu LW, Liu YJ, Leng JS, Du SY. Post microbuckling mechanics of fibre-reinforced shape-memory polymers undergoing flexure deformation. Mech Mater 2014;72:46–60.
[19] Lan X, Liu L, Liu Y, Leng J. Thermomechanical properties and deformation behavior of a unidirectional carbon-fiber-reinforced shape memory polymer composite laminate. J Appl Polym Sci 2019;137(14).
[20] Gall K, Mikulas M, Munshi NA, Beavers F, Tupper M. Carbon fiber reinforced shape memory polymer composites. J Intell Mater Syst Struct 2016;11(11):877–86.
[21] Liu Y, Du H, Liu L, Leng J. Shape memory polymers and their composites in aerospace applications: a review. Smart Mater Struct 2014;23(2).
[22] Wang Y, Li X. 4D-printed bi-material composite laminate for manufacturing reversible shape-change structures. Compos B Eng 2021;219:108918.
[23] Herath HM, Epaarachchi JA, Islam MM, Leng J. Carbon fibre reinforced shape memory polymer composites for deployable space habitats. Engineer: J Inst Eng 2019;52(1).
[24] Zhao H, Lan X, Liu L, Liu Y, Leng J. Design and analysis of shockless smart releasing device based on shape memory polymer composites. Compos Struct 2019;223.
[25] Lan X, Liu L, Zhang F, Liu Z, Wang L, Li Q, et al. World's first spaceflight on-orbit demonstration of a flexible solar array system based on shape memory polymer composites. Science China Sci China Technol Sc 2020;63(8):1436–51.
[26] Tiwari N, Shaikh AA. Micro-buckling of carbon fibers in shape memory polymer composites under bending in the glass transition temperature region. Curved Layer Struct 2021;8(1):96–108.
[27] Leng J, Wu X, Liu Y. Effect of a linear monomer on the thermomechanical properties of epoxy shape-memory polymer. Smart Mater Struct 2009;18(9).
[28] Saint-Venant Bd. Mémoire sur la torsion des prismes. Mémoires des Savants étrangers 1855;14:233–560.
[29] Tollmien W, Schlichting H, Görtler H, Riegels F. Zur Torsion von prismatischen Stäben. Ludwig Prandtl Gesammelte Abhandlungen: Springer; 1961. p. 79–80.
[30] Pineda EJ, Ricks TM, Bednarcyk BA, Arnold SM. Benchmarking and performance of the NASA multiscale analysis tool. AIAA scitech 2021 forum. 2021. p. 1351.
[31] Carrera E, Petrolo M, Nagaraj M, Delicata M. Evaluation of the influence of voids on 3D representative volume elements of fiber-reinforced polymer composites using CUF micromechanics. Compos Struct 2020;254:112833.